V European Conference on Computational Fluid Dynamics
ECCOMAS CFD 2010
J. C. F. Pereira and A. Sequeira (Eds)
Lisbon, Portugal,14-17 June 2010

# MECHANICAL AND THERMAL FLUID STRUCTURE INTERACTION OF NON-CONTACTING GAS SEALS IN JET ENGINES

**Y. Du[*] and M. Schäfer[†]**

[*] [†]Graduate School of Computational Engineering and
Institute of Numerical Methods in Mechanical Engineering
Technische Universität Darmstadt
64293, Darmstadt, Germany
[*]e-mail: duly@gsc.tu-darmstadt.de
[†]e-mail: schaefer@fnb.tu-darmstadt.de

**Key words:** Fluid structure interaction, Labyrinth seals, Heat transfer, Centrifugal effects, Fluid force induced vibration, Gas turbine

**Abstract.** *The mechanical and thermal fluid structure interaction (FSI) of labyrinth seals, which are a type of non–contacting gas seal commonly seen in gas turbines, are investigated in this paper. The fluid solver and the solid solver are coupled in a two–way implicit fashion. Two numerical cases are presented for different FSI effects. In the first case, the fluid force induced vibration of the structure is studied. The results reveal the dependency of vibration amplitudes on fluid inlet/outlet pressure. In the second case, thermal and centrifugal effects are simulated using FSI. The results indicate that various FSI models and CFD simulations can lead to significantly different thermal and mechanical predictions. The FSI effects in these studies are beyond the capability of single field analysis. All the seal configurations and operating conditions are based on experiments and close to reality.*

## 1 INTRODUCTION

Labyrinth seals are the most common and most important seals in modern jet engines. They provide non-contacting sealing at stationary/rotating surfaces, and their leakage flow is a main source of losses. Thus reducing the leakage is significant to the engine performance in terms of decreased specific fuel consumption and increased available thrust. As a result of the narrow flow path and the high speed turbulent flow, fluid structure interaction (FSI) plays a dominant role in labyrinth seals, such as fluid force induced vibration, and heat transfer between the flow and the structure. However, the FSI in labyrinth seals has not been studied in its full complexity. Separate CFD and FEM simulations employing additional simplifications are usually used to approximate the FSI effects. Therefore, numerical simulations of the fully coupled FSI effects are needed to improve our understanding of labyrinth seals.

Over the past years, FSI has attracted growing interests, and has become one of major focuses in the field of computational engineering[1]. Huge progress has been made in numerical methods of FSI, which allows FSI implementation in industrial cases at affordable computational costs.

In the current study, various FSI effects in labyrinth seals are presented. First, the fluid forced induced vibration is studied using 3D transient FSI simulations. Then, thermal and centrifugal effects are investigated on a rotating labyrinth seal of different configuration. Two–way implicit FSI approach is applied in both cases.

We shall use the multi–physics software package ANSYS® in this study. The algebraic multigrid CFD solver ANSYS CFX® and the FEM based structural solver ANSYS Mechanical™ are coupled without a third–party interface[4].

## 2 FSI APPROACH

Generally, there are two main approaches for FSI problems: the monolithic approach, which solves the governing equations of the fluid and the solid in a single solver; and the partitioned approach, which in contrast solves the governing equations separately in two distinct solvers. The partitioned approach can be divided into two main categories, which are one–way and two–way coupling. One–way coupling refers to the case where the data transfer is unidirectional, and two–way coupling means bidirectional data transfer. Two–way coupling can be further divided into explicit and implicit method. In the former case, data is exchanged only once per timestep, while in the latter case, it allows for several FSI iterations within each timestep till convergence is reached.

The monolithic approach has the advantage in robustness, but requires an extra code for the combined governing equations. In comparison, the partitioned approach is preferred on more occasions due to its better compatibility with existing high–efficient CFD and CSM codes. One–way coupling is only capable of representing weakly coupled physics, and is commonly used in thermal–stress analysis. When the fluid and the solid significantly affect each other, two–way coupling is needed. Furthermore, explicit methods usually deliver less accurate results and suffer from stability problems. In contrast, implicit methods are more favorable in academic FSI investigations. For these reasons, the implicit partitioned approach of two–way FSI is adopted in the current study.

In the FSI approach of ANSYS, the fluid mesh is deformed using mesh displacement models. The displacement received by the fluid solver on domain boundaries are diffused to other mesh points inside the domain by solving the displacement diffusion equation $\nabla \bullet (\Gamma_{disp} \nabla \delta) = 0$, where $\delta$ is displacements relative to the previous mesh locations, and $\Gamma_{disp}$ is called mesh stiffness. The solver provides several options for $\Gamma_{disp}$, such as *Increase near Small Volumes* $\Gamma_{disp} = \left(\frac{1}{V}\right)^{C_{stiff}}$, with $C_{stiff}$ being the exponent of mesh stiffness model.

## 3 FSI CASE I – FLUID FORCE INDUCED VIBRATION

The fluid force induced vibration of a non–rotating, room temperature, straight–through labyrinth seal is presented. Here we focus on the mechanical FSI effects, hence the fluid–solid surface is treated as a movable adiabatic wall.

### 3.1 Numerical models

The geometry and boundary conditions of the fluid model (Fig. 1) are based on experiments[2]. The working fluid is compressible air governed by ideal gas law. The inlet total temperature $T_{tot,in}$ is set at room temperature. Both inlet total pressure $p_{tot,in}$ and outlet static pressure $p_{stat,out}$ are varied to yield various pressure ratios. The validity of the standard $k-\varepsilon$ turbulence model used here for straight–through labyrinth seals has been repeatedly demonstrated in references. The mesh density and the near–wall element size are verified, resulting in a mesh of 1.7 million hexahedral elements.

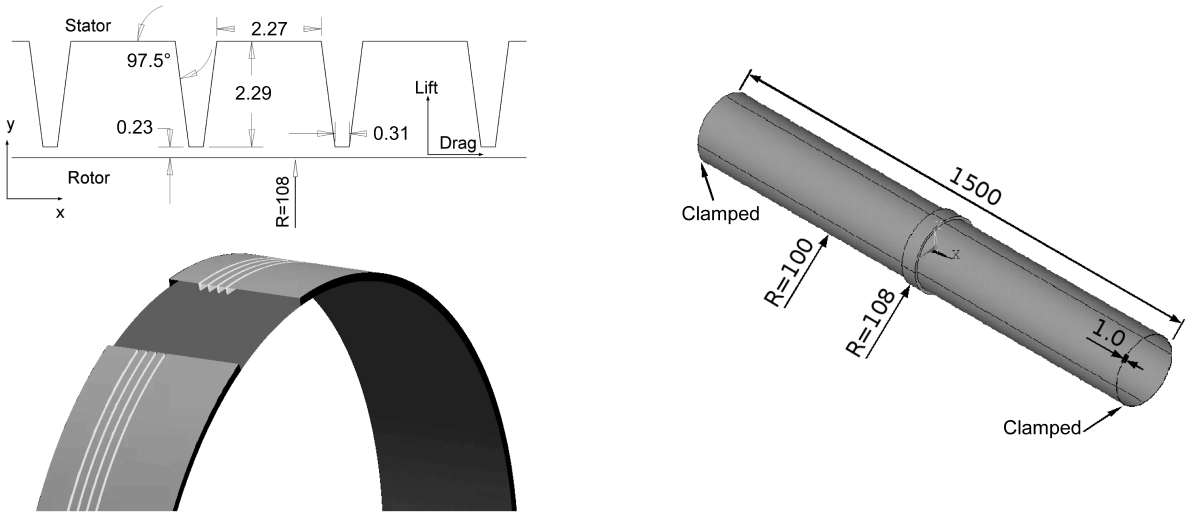


Figure 1: Fluid model (left) and rotor model (right) of the straight–through labyrinth seal (mm)

Since this work focuses on the rotor vibration, modeling of the stator is neglected here. The rotor is simplified as a disk fixed on a thin wall shaft (Fig. 1). The small deformation justifies a linear analysis with linear elastic material law. The material is steel with the density of 7806 kg/m$^3$, Young's modulus of $2.078 \times 10^{11}$ Pa, and Poisson's ratio of 0.3. The two ends of the shaft are clamped. Besides, the shaft is modeled with the second order thin wall pipe element, *PIPE16*.

Forces and displacements are transferred across the fluid–solid surface located in the middle of the shaft. Specifically, the structure is deformed by fluid pressure, and sends displacements back to the fluid. The mesh stiffness model is chosen as *Increase near Small Volumes* with $C_{stiff} = 1$.

### 3.2 Results and discussions

First, CFD analysis of the fluid field reveals the following features (Fig. 2): 1. There is a major vortex structure in each cavity; 2. The velocity increases across the seal and reaches its maximum at the last tip; 3. The static pressure is homogeneously distributed in each cavity, and decrease as the flow accelerates.

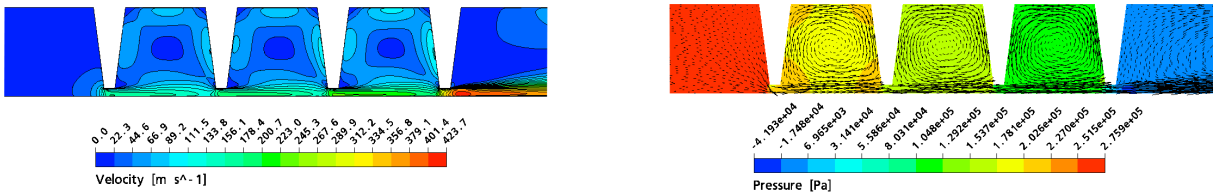


Figure 2: Velocity field and static pressure field of the labyrinth seal (pressure drop = 276 kPa)

Turning now to the FSI results, to demonstrate that the vibration is due to fluid pressure rather than inertial forces, the fluid forces received by the rotor in the FSI simulations are applied as loads in the finite element analysis (FEA) of the rotor. As shown in Fig. 3, the structural displacements obtained by FSI and FEA are consistent.

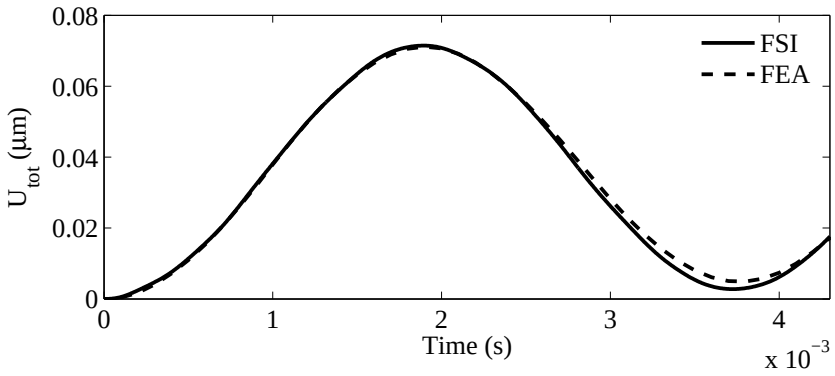


Figure 3: Structural displacements obtained with FSI and FEA

In Fig. 4, it shows the transient responses of the rotor displacement and the lift force at the coupling surface. A periodic vibration can be recognized clearly. The rotor vibrates at a frequency of 274 Hz, which is almost the same as its first order of natural frequency. The amplitude is only about 0.03% of the tip clearance.

The dependency of the amplitude on pressure ratio $\pi$ and mass flow $\dot{m}$ are shown in Fig. 5 and Fig. 6, respectively. The pressure ratio is defined as $\pi = p_{tot,in}/p_{stat,out}$. In Fig. 5, $p_{stat,out}$ is fixed at the atmospheric pressure and $p_{tot,in}$ is varied to obtain various $\pi$. In Fig. 6, $\pi$ is maintained at 2, whereas $p_{tot,in}$ and $p_{stat,out}$ are varied proportionally

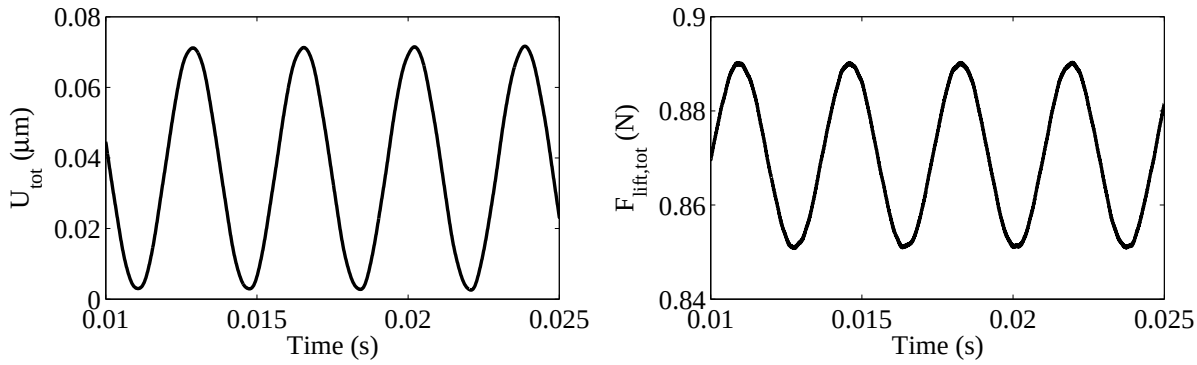


Figure 4: Displacement history (left) and lift force history (right) ($\pi = 3.8$, $\dot{m} = 0.088$ kg/s)

to obtain various $\dot{m}$. The amplitude increases linearly with $\pi$ and $\dot{m}$. The maximum amplitude is about 0.05% of the tip clearance.

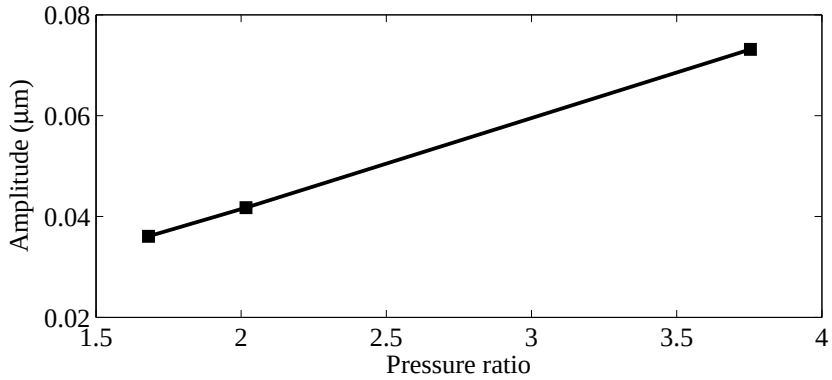


Figure 5: Influence of pressure ratio $\pi$ on the amplitude of rotor vibration, $p_{stat,out} = 1$ atm

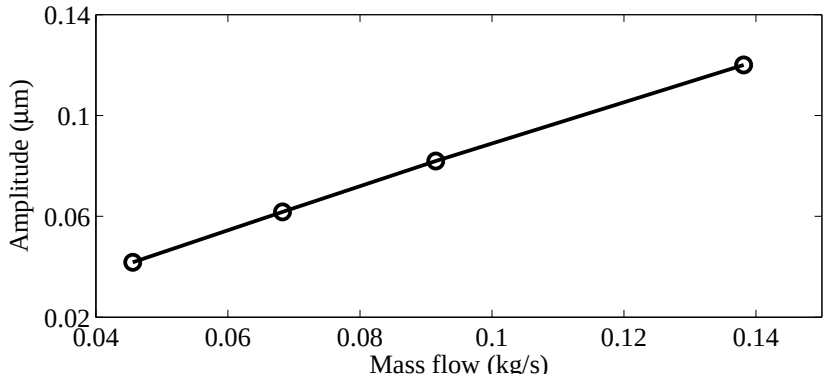


Figure 6: Influence of $\dot{m}$ on the amplitude of rotor vibration, $\pi = 2$

## 4 FSI CASE II – THERMAL AND CENTRIFUGAL EFFECTS

The thermal and centrifugal effects of an axisymmetric, high temperature, rotating stepped labyrinth seal is investigated. This case focuses on: 1. Comparison of various FSI and CFD models; 2. Heat transfer behavior across fluid–structure surfaces.

### 4.1 Numerical models

Both fluid and structural models are based on room temperature rotating experiments[3]. Figure 7 shows the geometric parameters of the fluid domain. The outlet static pressure $p_{stat,out}$ is kept constant, while the inlet total pressure $p_{tot,in}$ and total temperature $T_{tot,in}$ are varied. Nonadiabatic wall boundary conditions are applied in thermal FSI simulations. Turbulence model will be discussed in more detail in section 4.2, where the $SST$ turbulence model is finally chosen. The mesh contains 102,000 hexahedral elements with one element in circumferential direction.

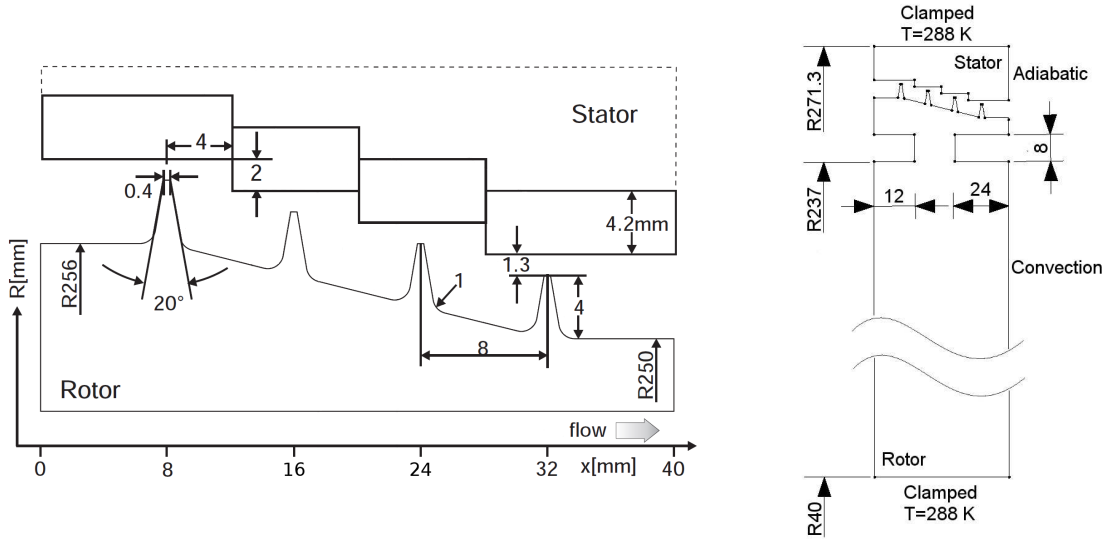


Figure 7: Fluid model (left) and solid model (right) of the stepped labyrinth seal (mm)[3]

In accordance to the experiment, titanium alloy, which is commonly seen in aeronautics, is applied in this study. Thermal property dependencies on temperature are shown in Tab. 1. Both rotor and stator are modeled with second order 3D coupled–field element, $SOLID226$. Each node has four DOFs: structural displacements $U_x$, $U_y$, $U_z$, and temperature. Moreover, the centrifugal effect is also enabled for this element type.

Data are exchanged at the fluid–rotor and fluid–stator surfaces in FSI simulations. The coupling variables include mechanical quantities, i.e. displacement (DISP) and force (F), as well as thermal quantities, i.e. temperature (T) and heat flow (HF). Four different FSI models are employed here, and a brief overview is given in Tab. 2. In a TFSI analysis

| | 300 K | 600 K |
|---|---|---|
| Thermal conductivity | 7.3 W/m K | 10.9 W/m K |
| Specific heat capacity | 560 J/kg K | 640 J/kg K |
| (Secant) Thermal expansion | $8.6 \times 10^{-6}$ /K | $9.2 \times 10^{-6}$ /K |
| Density | 4430 kg/m$^3$ | |
| Young's modulus | $1.138 \times 10^{11}$ Pa | |
| Poisson's ratio | 0.342 | |

Table 1: Material properties of the rotor and the stator

with rigid structure, only thermal variables are coupled. Such approach is also known as Conjugated Heat Transfer (CHT) as available in some CFD software. In contrast, the TFSI model with elastic structure is more realistic. In both one–way and two–way CFSI models, only mechanical quantities are exchanged. They are distinguished from each other by including or excluding the influence of fluid forces on the structure. The fluid mesh is deformed using the *Increase near Small Volumes* mesh stiffness model with $C_{stiff} = 0.5$.

| FSI effects | Abbreviations | Sub–models | Coupled variables |
|---|---|---|---|
| Thermal | TFSI | Rigid structure | T, HF |
| | | Elastic structure | T, HF, DISP, F |
| Centrifugal | CFSI | One–way | DISP |
| | | Two–way | DISP, F |

Table 2: Various FSI models

These dimensionless numbers will be used in later sections: discharge coefficient $C_D = \dot{m}/\dot{m}_{id}$ describes the mass flow; windage heating coefficient $\sigma = c_p \cdot \Delta T_{tot}/\omega^2 R^2$ is related to the total temperature increase from inlet to outlet, where $\omega$ is rotational speed; circumferential Mach number $M_{tan} = \omega R/c$ indicates the rotational speed. More details can be found in the reference [3].

### 4.2 Verification and validation

First, various turbulence models are validated. Comparing to case I, the fluid domain of the current stepped labyrinth seal is more complex. It is known that the standard $k-\varepsilon$ is less accurate when there are flow separation and recirculation. In Fig. 8, model results are compared with respect to discharge coefficient at growing pressure ratio. It is shown that both SST and RNG $k-\varepsilon$ lead to less than 3% deviation from test results, and the former is slightly better. Therefore, SST is applied in the following study.

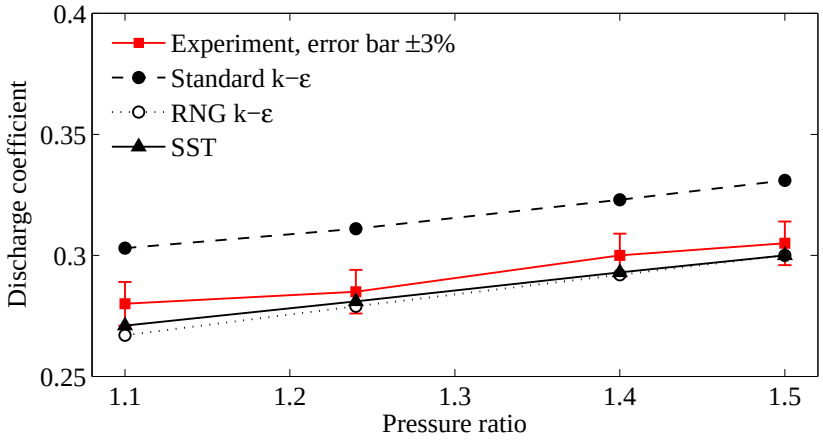


Figure 8: Validation of various turbulence models regarding leakage prediction (non–rotating, $T_{tot,in}$ = 300 K)

Then, velocity profiles at $x$ = 3 mm are compared with test results. In Fig. 9, it shows the distribution of dimensionless axial and circumferential velocity along the radial direction. The actual velocities are divided by the rotor surface speed, while the radial position is normalized by the channel height.

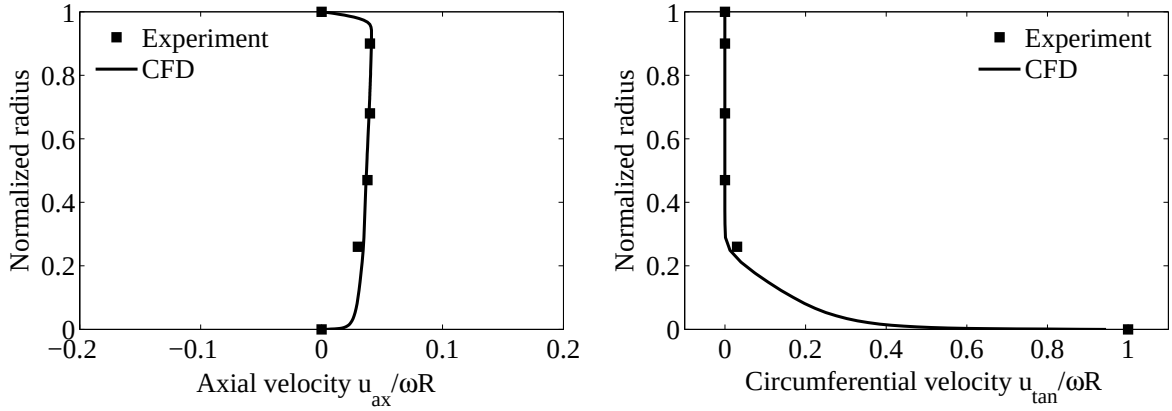


Figure 9: Velocity profiles at $x$ = 3 mm ($\pi$ = 1.05, $M_{tan}$ = 0.465, $T_{tot,in}$ = 300 K)

The structural model is also validated. Centrifugal displacements at various locations of the rotor are compared with experimental results of the second tooth at growing rotational speed (Fig. 10). The numerical results suggest that the centrifugal growth of the rotor is very uniform. Moreover, the FEA prediction shows good agreement with measurements.

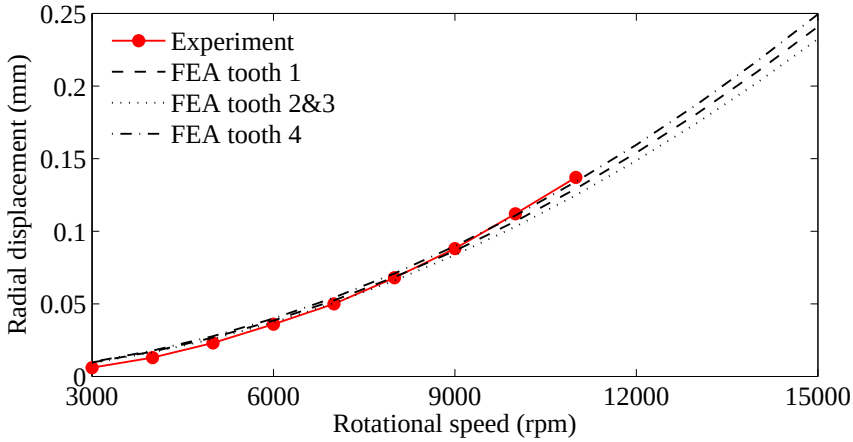


Figure 10: Radial centrifugal displacements at the rotor teeth

### 4.3 Results and discussions

Detailed flow features are presented in Fig. 11. A large vortex between the two teeth can be recognized. Above the vortex, there are a major and a secondary recirculation zones behind and in front of the step, respectively. Figure (b) shows that the circumferential velocity increases from zero at the upper stationary wall to its maximum at the lower rotating wall. Moreover, the static temperature is raised across the seal, which is mainly due to friction at the rotating wall.

Next, a series of parameter studies is conducted in order to compare FSI and CFD. Dimensionless numbers are calculated using CFD and various FSI models, where the operating conditions are varied.

In Fig. 12, the mass flow is plotted as the corresponding dimensionless number, discharge coefficient $C_D$, versus the pressure ratio. $C_D$ is found to increase with $\pi$, which accords with previous research. At both $T_{tot,in}$ = 300 K and 600 K, CFSI and TFSI with elastic structure result in smaller $C_D$ than CFD. This can be attributed to the reduction of tip clearance due to centrifugal growth and thermal expansions. Moreover, the gap between CFSI and CFD predictions is independent from $\pi$, as can be recognized from the parallel curves. This result can be explained by the constant rotational speed. Since the centrifugal growth is dominated by rotational speed in CFSI simulations, the tip clearance change is constant in the current case, and the change of $C_D$ is thus constant. At $T_{tot,in}$ = 600 K, thermal expansion becomes more significant, hence TFSI with elastic structure yields the smallest $C_D$. In addition, TFSI with rigid rotor is the same as CFD at low $T_{tot,in}$, and shows a difference from CFD at high $T_{tot,in}$.

Figure 13 shows the influence of circumferential Mach number $M_{tan}$, which indicates the rotational speed, on the windage heating coefficient $\sigma$, which represents the total temperature increase across the seal. It is apparent that $\sigma$ increases with rotational

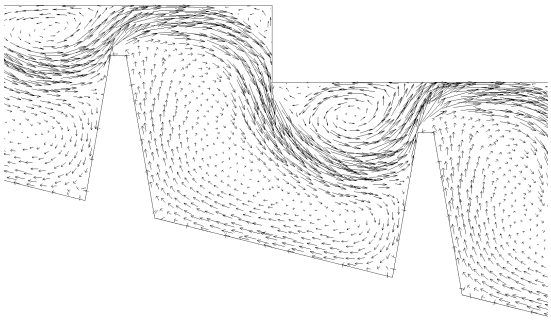

(a) Axial–radial velocity

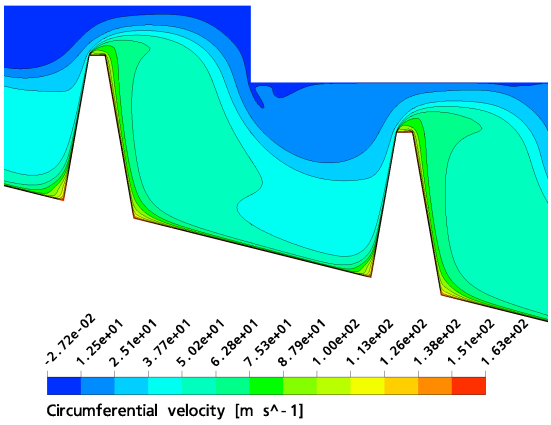


(b) Circumferential velocity

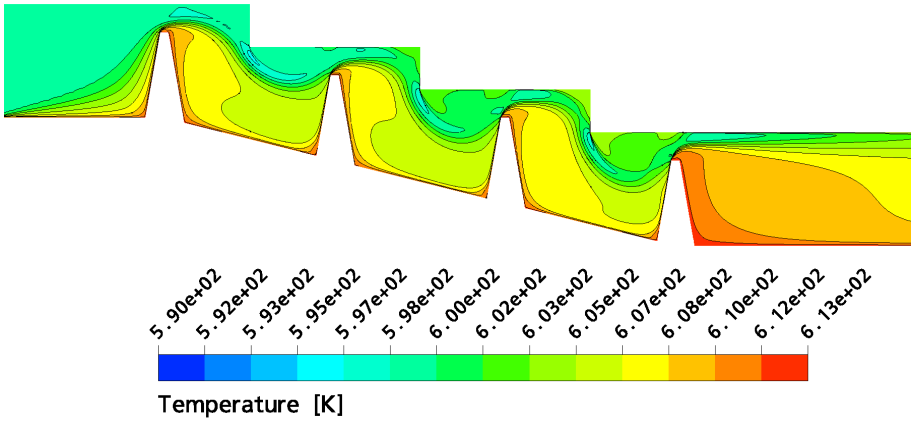


(c) Static temperature

Figure 11: Flow features of the stepped labyrinth seal ($\pi = 1.1$, $M_{tan} = 0.458$, $T_{tot,in} = 600$ K)

speed. CFSI leads to slightly larger $\sigma$ than CFD. This can be attributed to the decrease in tip clearance and consequently the increase in wall friction. The curves of CFD and CFSI are not parallel, since the tip clearance in CFSI simulations is affected by rotational speed. Besides, when $T_{tot,in} = 300$ K, both TFSI models are coincident with each other and lead to low $\sigma$, because the heat generated by wall friction is in part absorbed by the solid.

Figure 14 illustrates the structural temperature field and radial thermal expansion at $T_{tot,in} = 600$ K. It can be recognized that the highest temperature occurs at the rotor teeth. In contrast, the stator has obviously lower temperature due to the stationary walls. Furthermore, the figures indicate that the thermal expansion of the stator is small and can be neglected compared to the rotor. This can be explained by the large temperature gradient and large height of the rotor.

In Fig. 15 and Fig. 16, the temperature distribution and the mean Nusselt number $\bar{Nu}$ at FSI surfaces are demonstrated for the rotor and the stator, respectively. Meanwhile,

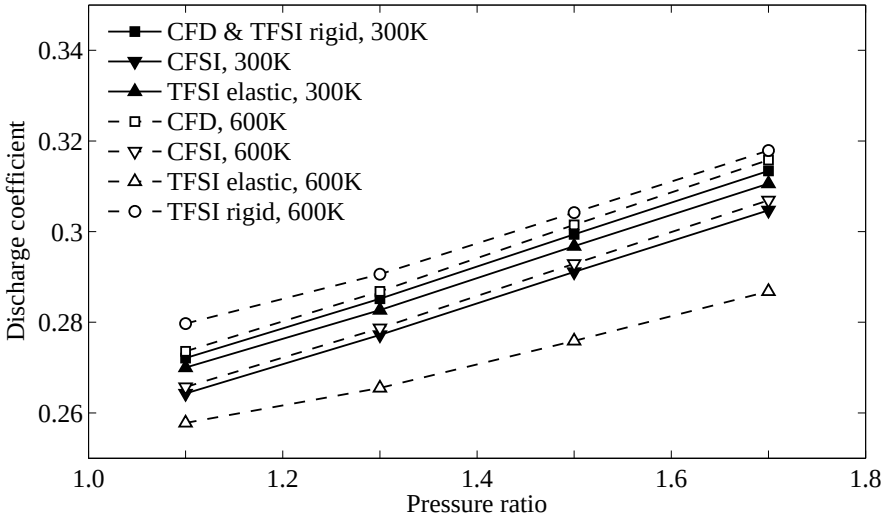


Figure 12: Influence of pressure ratio on discharge coefficient ($M_{tan} = 0.458$, $T_{tot,in} = 300$ K/600 K)

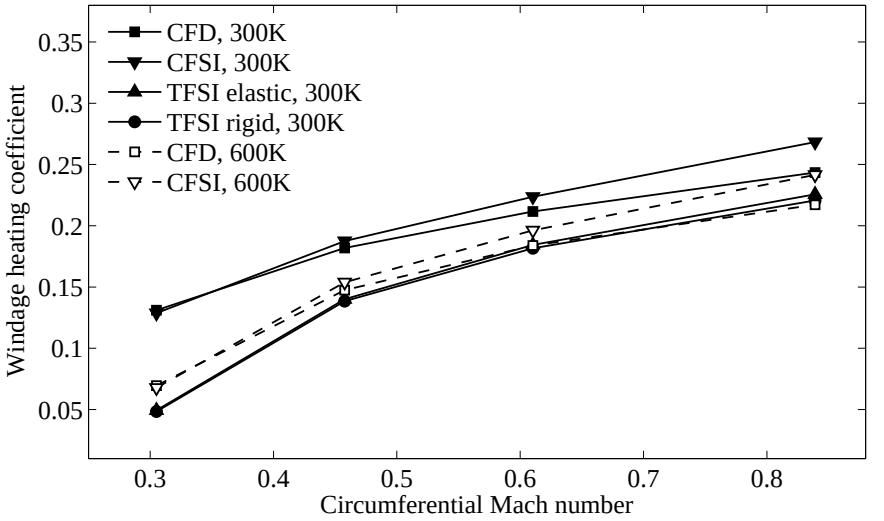


Figure 13: Influence of rotational speed on windage heating coefficient ($\pi = 1.5$, $T_{tot,in} = 300$ K/600 K)

the pressure ratio condition is varied.

There are clear temperature peaks at the tooth tips on the rotor (Fig. 15). Moreover, the peak values decrease from the second tooth to the fourth tooth. Overall, the rotor temperature increases with $\pi$. TFSI with elastic structure results in large $\bar{Nu}$ of the rotor in comparison to TFSI with rigid structure.

Comparing to the rotor, the temperature in the stator is lower by about 100 K. The explanation for this is that there is less frictional heat generated at stationary walls. Sudden increase in temperature can be recognized at each step, and the temperature is

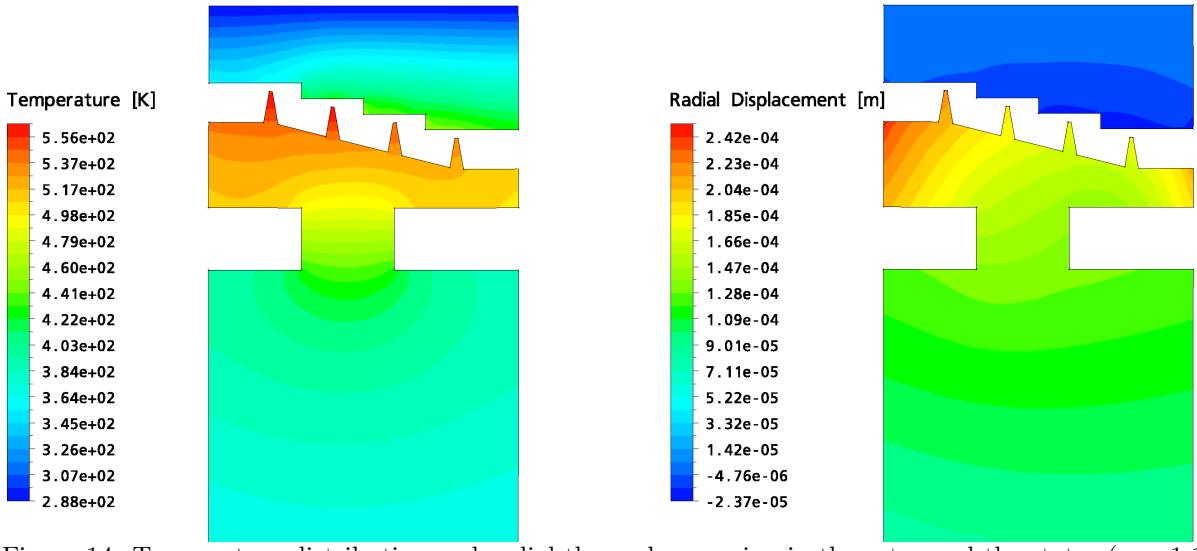


Figure 14: Temperature distribution and radial thermal expansion in the rotor and the stator ($\pi = 1.1$, $M_{tan} = 0.458$, $T_{tot,in} = 600$ K)

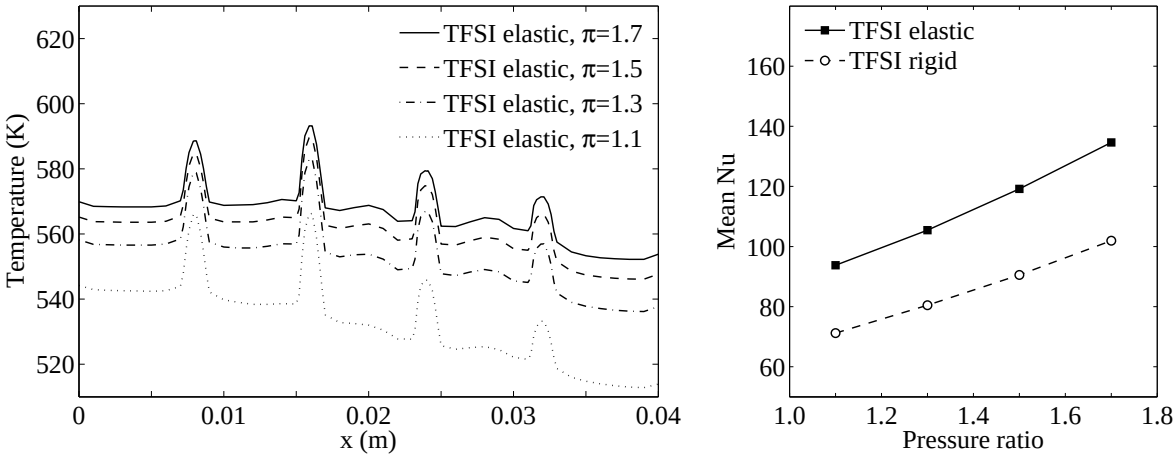


Figure 15: Structural temperature distribution across the labyrinth seal (left) and mean Nusselt number (right) of the rotor ($M_{tan} = 0.458$, $T_{tot,in} = 600$ K)

elevated from the inlet to the outlet. High $\pi$ enhances the stator temperature obviously. The $\bar{Nu}$ of the stator is found to increase with $\pi$ significantly. Similar to the rotor, TFSI model with elastic structure leads to larger stator $\bar{Nu}$ than its rigid counterpart.

## 5 CONCLUSIONS

Various mechanical and thermal FSI effects of labyrinth seals are studied using a two–way implicit approach. First, the fluid force induced vibration of the rotor is simulated. The results indicate linear relationships between the amplitude and the pressure ratio/mass flow. Then, the thermal and centrifugal effects in a rotating stepped labyrinth

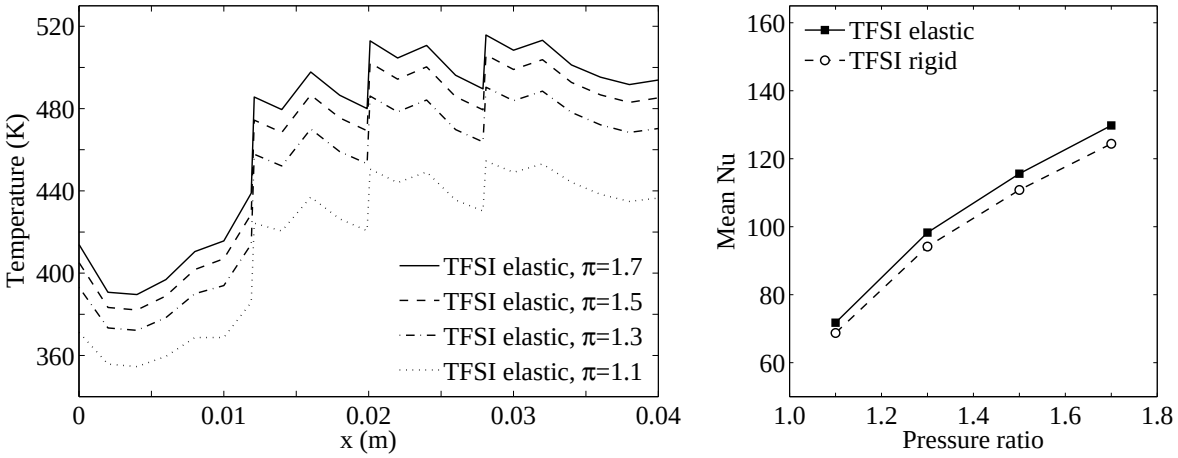


Figure 16: Structural temperature distribution across the labyrinth seal (left) and mean Nusselt number (right) of the stator ($M_{tan} = 0.458$, $T_{tot,in} = 600$ K)

seal are studied. The CFD model and the CSM model show excellent agreement with experimental results. It is found that CFD and various FSI models lead to distinctively different results in some cases. In addition, the heat transfer across fluid–solid interfaces is presented.

The findings of this study enhance our understanding of the FSI effects in labyrinth seals. On the one hand, the coupled physics beyond CFD/CSM analyses are simulated using FSI, such as fluid force induced vibration and heat transfer across fluid–solid surfaces. On the other hand, FSI simulations are found to lead to significantly different predictions comparing to the CFD analysis in some cases. Therefore, the readers are well advised to choose between various FSI models and traditional CFD models accordingly.

## ACKNOWLEDGMENT

The authors would like to thank the *Deutsche Forschungsgemeinschaft* for the financial support of this work within the *Graduiertenkolleg 1344: Instationäre Systemmodellierung von Flugtriebwerken* and the *Graduate School of Computational Engineering.*

## REFERENCES

[1] H. -J. Bungartz and M. Schäfer, Fluid–structure interaction – modelling, simulation, optimization, *Springer* (2006).

[2] M. P. Proctor and I. R. Delgado, Leakage and power loss test results for competing turbine engine seals, *NASA/TM-2004-213049, ASME Paper No. GT2004-53935* (2004).

[3] J. Denecke, K. Dullenkopf, S. Wittig and H. -J. Bauer, Experimental investigation

of the total temperature increase and swirl development in rotating labyrinth seals, *ASME Paper No. GT2005-68677* (2005).

[4] ANSYS® Academic Research, Release 11.0, Help System, ANSYS, Inc..